Calibration of wind turbine lifting line models from rotor loads

Carlo L. Bottasso [a,b,*], Stefano Cacciola [b], Xabier Iriarte [c]

[a] Wind Energy Institute, Technische Universität München, Boltzmannstraße 15, Garching D-85748, Germany
[b] Dipartimento di Scienze e Tecnologie Aerospaziali, Politecnico di Milano, Via La Masa 34, Milano I-20156, Italy
[c] Departamento de Ingeniería Mecánica, Energética y de Materiales, Universidad Pública de Navarra, Pamplona E-31006, Spain

Article history:
Received 2 May 2013
Received in revised form
8 October 2013
Accepted 10 November 2013
Available online 1 December 2013

1. Introduction and motivation

At present, several aerodynamic models for wind turbine rotors are based on the coupling of a lifting line with a model of the wake and of the surrounding flow. A lifting line describes a blade as a spanwise sequence of two-dimensional airfoils, typically characterized by their chord, twist and aerodynamic center position with respect to an arbitrary reference curve. Each airfoil is in turn characterized by its lift, drag and moment coefficients, which vary as functions of the angle of attack, Reynolds and possibly Mach numbers. The aerodynamic coefficients are either obtained experimentally from ad hoc wind tunnel tests (Althaus, 1988; Abbott and von Doenhoff, 1959) or computed numerically with specialized codes (for example, see Drela and Giles, 1987).

Different models are available for the coupling with lifting lines, depending on trade-offs among accuracy, modeling complexity, computational cost and final scope of the simulation. Possible choices range from blade element momentum (BEM) theory (Hansen, 2008; Schepers, 2012), dynamic and free wake models (Peters, 2009), or computation fluid dynamics (CFD) approaches, such as the ones based on large eddy simulation (LES) techniques (Wu and Porté-Agel, 2011; Churchfield and Lee, 2012). Such models currently cover many of the very different needs arising in the study and design of wind energy systems. These range from the computation of load spectra on a machine, typically implying in excess of 10^7 time steps and presently routinely carried out by using sophisticated variants of the BEM

* Corresponding author at: Wind Energy Institute, Technische Universität München, Boltzmannstraße 15, Garching D-85748, Germany. Tel.: +49 89 289 16680.
E-mail address: carlo.bottasso@tum.de (C.L. Bottasso).

Notation

A	rotor area
C_D	drag coefficient
C_F	thrust coefficient
C_L	lift coefficient
C_P	power coefficient
C_{Mx}	in-plane bending moment coefficient
C_{My}	out-of-plane bending moment coefficient
F	aerodynamic thrust
J	cost function
N	number of samples
P	aerodynamic power
R	rotor radius
V	wind speed
m	number of outputs
n	number of parameters
s_i	ith singular value
$\boldsymbol{F}$	Fisher information matrix
$\boldsymbol{G}$	sensitivity matrix of outputs with respect to parameters
$\boldsymbol{M}$	square root of Fisher matrix
$\boldsymbol{R}$	error covariance matrix
$\boldsymbol{S}$	square matrix of singular values
$\boldsymbol{U}$	matrix of left singular vectors
$\boldsymbol{V}$	matrix of right singular vectors
$\boldsymbol{\Sigma}$	rectangular matrix of singular values
$\boldsymbol{n}$	vector of shape functions
$\boldsymbol{p}$	vector of physical parameters
$\boldsymbol{r}$	residual vector
$\boldsymbol{y}$	output vector
$\boldsymbol{z}$	measurement vector
$\boldsymbol{\psi}$	vector of eigenshapes
$\boldsymbol{\theta}$	vector of statistically independent parameters
$\boldsymbol{\Delta}$	corrective function
$\boldsymbol{\Omega}$	rotor speed
α	angle of attack
β	blade pitch
$\chi_{p,q}$	correlation between pth and qth parameters
η	non-dimensional spanwise coordinate
λ	tip speed ratio
ρ	air density
σ	standard deviation
$d_{p,q}$	element p, q of Fisher matrix inverse
$(\cdot)^*$	estimated quantity
$(\cdot)^0$	nominal quantity
$(\cdot)^T$	transpose
$(\cdot)_{\mathrm{ID}}$	identifiable quantity
$(\cdot)_{\mathrm{NID}}$	non-identifiable quantity
$(\bar{\cdot})$	true (unknown) quantity
BEM	blade element momentum
CFD	computational fluid dynamics
LES	large eddy simulation
ML	maximum likelihood
RANS	Reynolds averaged Navier–Stokes
SQP	sequential quadratic programming
SVD	singular value decomposition
TSR	tip speed ratio

approach, all the way to the generation of turbulent flow fields within a wind farm, for which LES methods are the current method of choice (Churchfield et al., 2012; Fleming et al., 2013).

In all these lifting-line-based approaches, the coupled model provides for a description of the flow field around the rotor. This, in addition to the knowledge of the instantaneous environmental wind and blade-motion-induced speed, allows for the computation of the local angle of attack and of the relevant fluid dynamic parameters at any point along the lifting line. From this information, using the available airfoil aerodynamic coefficients, one can generate the local lift, drag and moment at the corresponding blade cross section, which are in turn fed back as driving forces to the coupled flow model. Iterations are carried out between the coupled flow model and the lifting line, until the flow kinematics is coherent with the loading, according to the used model.

The ability of such approaches to accurately compute all quantities of interest relies on whether the models are capable of capturing the relevant physics, on an adequate spatial and temporal resolution of the solution scales, and on the correct tuning of all physical parameters. System identification (or, more precisely, parameter estimation) techniques are available to calibrate parameters in mathematical models of physical systems from available experimental observations of relevant quantities (Ljung, 1999).

This work deals with the calibration of aerodynamic models for wind turbine rotors, and it is in particular concerned with the estimation of lifting line airfoil aerodynamic characteristics. These may differ from nominal assumed ones for a variety of reasons: shape defects due to manufacturing imperfections, erosion, dirt or ice formation; imprecisions during their two-dimensional characterization because of experimental or numerical defects; lack of two-dimensionality, uncorrected by other means in the model (on account for example of Coriolis effects in the root region, cross-flow due to blade sweep, or other reasons).

Goal of this work is the development of methods that can correct available baseline airfoil characteristics, using measured rotor data. In fact, it is clear that the loads generated on a rotor, at the hub and along the blades, depend on the aerodynamic characteristics of the airfoils. Hence one can hypothesize that, by using measured quantities such as rotor power and thrust and blade loads, the local characteristics of its airfoils could be inferred. The problem is difficult because of the possible low observability of the parameters of interest, since airfoil characteristics in some sections of the blade might have small effects on the measured quantities. Furthermore, as it is often the case in identification problems, some parameters may have effects on the measurements that are similar to the ones of other parameters, so that their respective characteristics may be difficult to discern and separate from one another.

To deal with these problems, the method presented in this work has been designed accordingly. To account for the inevitable presence of various sources of errors and noise in the measurements, the approach is based on a maximum likelihood formulation that can account for sensor and process noise. Furthermore, to ease the understanding of the well posedness of the problem and the choice of a set of identifiable parameters, the method makes use of a singular value decomposition (SVD) approach (Golub and van Loan, 1996; Lancaster and Tismenetsky, 1985). By this method, the physical parameters of interest, which represent corrections to the baseline lift and drag characteristics of the airfoils, are recast in terms of a new set of statistically independent parameters. This reformulation of the problem presents two key advantages: first, one has a simple way of selecting only those parameters that are associated with a desired level of confidence; second, by visual inspection of the eigenshape functions associated with the new parameters, one can understand which physical characteristics of the blade airfoils can be reliably identified from a given set of available measurements.

There are at least two main possible application areas of the methodology proposed here. In the first, one extracts local airfoil information from numerical simulations; for example, given CFD results on the full rotor, one could estimate the local airfoil characteristics in complex three-dimensional regions at the root and tip of the blade. Similar ideas have been previously described in Bak et al. (1999). In the second application area, one estimates airfoil properties from experimental measurements performed on a rotor. Conceptually, the measurements could be performed in the field, on a suitably instrumented machine and with an appropriate processing of the raw data. In this paper, on the other hand, the technique is applied to a scaled rotor model tested in the wind tunnel of the Politecnico di Milano. In fact, wind tunnel testing can be used for the validation and calibration of mathematical models of wind energy systems, supporting accurate measurements of problems in aerodynamics, aeroservoelasticity and control under known boundary conditions (Bottasso et al., 2013b).

The scaled wind turbine used in this study was tested in a number of operative conditions spanning a suitable range of angles of attack at the blade airfoils. From such measurements, the airfoil characteristics were identified using the method described in this paper. Significant mismatches with respect to the nominal properties of the airfoils were detected. These were traced back to manufacturing imprecisions due to the very small scale of the model, as well as to a significant sensitivity of the airfoil performance to transition strip geometry and testing conditions at the low Reynolds of the experiments. The improved lifting lines were then used in a variety of validation activities, of which two examples are given here.

In a first aerodynamic application, the updated airfoil characteristics were used for a combined lifting-line-LES simulation of the wind turbine model and its wake (Schito, 2011), as shown in Fig. 1. The computational domain comprised the whole wind tunnel test section, including the turbulence and roughness elements used to generate a turbulent boundary layer. In turn, the results of the simulation were used for validating the approach in its ability to predict the wind turbine wake structure, turbulence intensity and speed deficit, by comparison with hot wire measurements.

In a second aeroelastic application, the updated airfoil characteristics were used for the simulation of emergency shut-downs following a grid loss (Bottasso et al., 2013b). Several different open loop pitch profiles were tested in the wind tunnel, obtaining measured responses during the aerodynamic braking operations that differed in the maximum overspeed and peak loads at the tower base. The same pitch profiles were used for aeroelastic simulations of the shut-down procedures, obtaining the excellent correlations between experimental and simulation responses shown in Fig. 2.

In both cases, lifting lines of good quality and with a tuning of their parameters that actually reflected their airfoil performance were instrumental for the achievement of good simulation results and the final validation of the computational tools.

The paper is organized as follows. Section 2 describes the proposed approach, and starts by formulating the estimation problem as a maximum likelihood optimization. Next, the SVD approach is introduced as a way of robustifying the formulation,

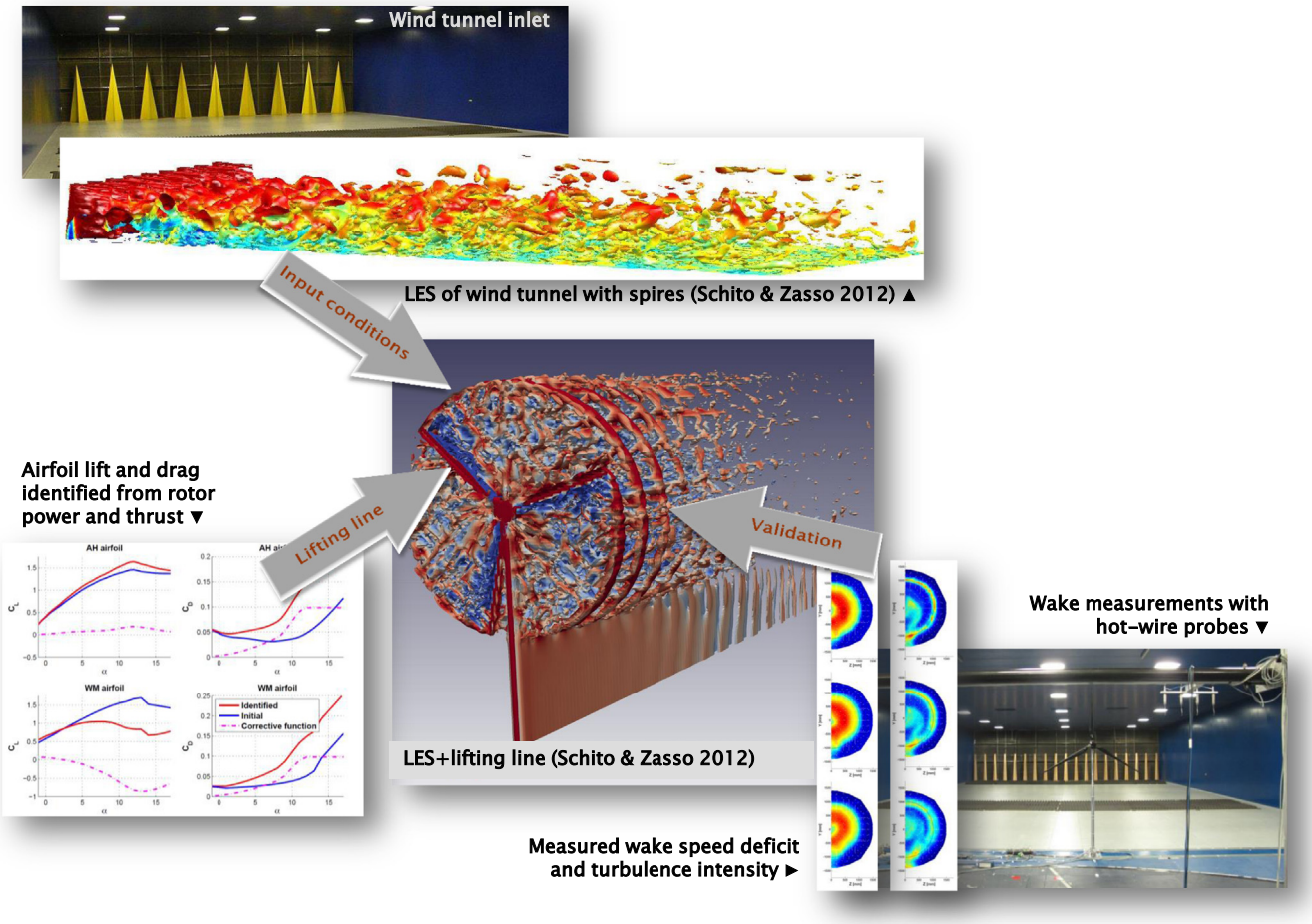

Fig. 1. LES simulation of a scaled wind turbine model in a wind tunnel, using experimentally calibrated lifting lines, and comparison with experimental wake measurements.

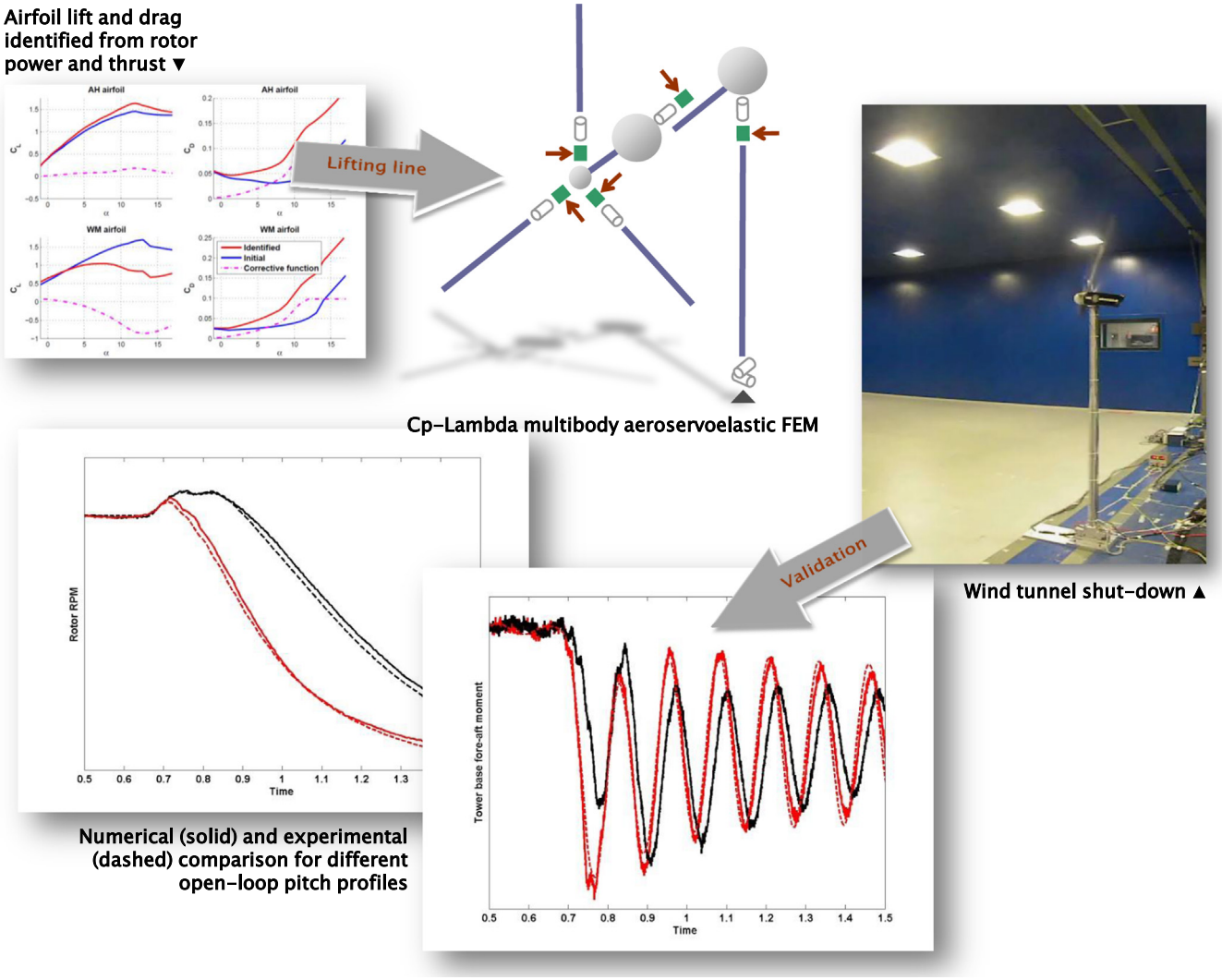

Fig. 2. Multibody simulation of emergency shut-downs of a scaled wind turbine model in a wind tunnel, using experimentally calibrated lifting lines, and comparison with experimental measurements. Solid lines: simulation; dashed lines: experimental values; red (lighter) lines: higher initial pitch rate; black (darker) lines: lower initial pitch rate.

by addressing the problem of well-posedness and identifiability. The section is concluded by the definition of the estimation parameters, of the constraints and of the outputs associated with the available measurements. Results are presented in Section 3. At first, the estimation of the airfoil properties of a scaled wind turbine model is presented; the direct use of physical quantities is shown to be ill-posed in this case, due to the collinearity of some parameters, while the SVD-based approach overcomes the problem and leads to the identification of a good quality lifting line model. Finally, the effects of multiple spanwise load measurements are illustrated by means of a simulation study; as expected, such additional measurements allow for a better distinction of the characteristics of the different airfoils than in the case when only hub measurements are available. Conclusions and outlook are given in Section 4.

2. Formulation

2.1. Maximum likelihood estimation

Consider a BEM model of the aerodynamics of a wind turbine (Hansen, 2008). The model is noted $\mathcal{M}(\boldsymbol{p})$, where $\boldsymbol{p} \in \mathbb{R}^n$ is a vector of free physical parameters that need to be estimated from available measurements. In the present work, parameters $\boldsymbol{p}$ are related to the aerodynamic lift and drag characteristics of the rotor blade airfoils, as more precisely described later on. Because of the inevitable presence of noise in the measurements, the unknown parameters collected in vector $\boldsymbol{p}$ are to be regarded as stochastic variables.

Given some output quantities $\boldsymbol{y} = \boldsymbol{h}(\boldsymbol{p})$, $\boldsymbol{y} \in \mathbb{R}^m$, their experimentally measured quantities $\boldsymbol{z}$ can be expressed as

$$\boldsymbol{z} = \boldsymbol{y} + \boldsymbol{r}, \tag{1}$$

where the residual $\boldsymbol{r}$ is due to both measurement and modeling errors, the latter caused by modeling approximations or unresolved physics in $\mathcal{M}$.

Given $\boldsymbol{p}$, the probability of the experimental observation $\boldsymbol{z}_i$ is noted $p(\boldsymbol{z}_i|\boldsymbol{p})$. Having a sample of observations $S = \{\boldsymbol{z}_1, \boldsymbol{z}_2, \ldots, \boldsymbol{z}_N\}$, the likelihood function of the set is defined as

$$f(S, \boldsymbol{p}) = \prod_{i=1}^{N} p(\boldsymbol{z}_i|\boldsymbol{p}), \tag{2a}$$

$$f(S, \boldsymbol{p}) = ((2\pi)^m \det \boldsymbol{R})^{-N/2} \exp\left(-\frac{1}{2}\sum_{i=1}^{N} \boldsymbol{r}_i^T \boldsymbol{R}^{-1} \boldsymbol{r}_i\right), \tag{2b}$$

where the second expression assumes white and zero mean residuals. The error covariance is noted $\boldsymbol{R}$, where $E[\boldsymbol{r}_i \boldsymbol{r}_j^T] = \boldsymbol{R}\delta_{ij}$, $E[\cdot]$

being the expected value operator and δ_{ij} the Kronecker delta symbol. If modeling errors are present, the assumption of zero mean residuals might not be fully satisfied, although it is often used in practical applications (Jategaonkar, 2006).

A maximum likelihood (ML) estimate $\boldsymbol{p}^*$ of the free parameters is obtained by maximizing function $f(S,\boldsymbol{p})$ or, equivalently, minimizing its negative logarithm

$$\boldsymbol{p}^* = \arg\min_{\boldsymbol{p}} J, \tag{3}$$

where

$$J = -\ln f(S,\boldsymbol{p}), \tag{4a}$$

$$J = \frac{Nm}{2}\ln 2\pi + \frac{N}{2}\ln\det \boldsymbol{R} + \frac{1}{2}\sum_{i=1}^{N} \boldsymbol{r}_i^T \boldsymbol{R}^{-1}\boldsymbol{r}_i. \tag{4b}$$

A robust implementation of problem (3) can be based on the following iteration (Klein and Morelli, 2006; Bottasso et al., 2013a):

1. Assuming a temporarily frozen error covariance $\boldsymbol{R}$, minimize with respect to $\boldsymbol{p}$ the cost
$$\hat{J} = \frac{1}{2}\sum_{i=1}^{N} \boldsymbol{r}_i^T \boldsymbol{R}^{-1}\boldsymbol{r}_i, \tag{5}$$
which is obtained from Eq. (4b) by neglecting all irrelevant constants.
2. Assuming temporarily frozen parameters $\boldsymbol{p}$, minimize J with respect to $\boldsymbol{R}$, which gives (Jategaonkar, 2006)
$$\boldsymbol{R} = \frac{1}{N}\sum_{i=1}^{N} \boldsymbol{r}_i \boldsymbol{r}_i^T. \tag{6}$$
3. Return to step 1, and repeat until convergence.

This approach should be contrasted with the classical weighted least squares approach, which amounts to performing step 1 only once, by assuming $\boldsymbol{R}$ known and frozen.

To enhance conditioning, both parameters and outputs are non-dimensionalized by suitable reference quantities. Furthermore, to improve convergence towards physically meaningful solutions, bounds expressing upper and lower admissible values for the free parameters are appended to the optimization of step 1, which is in turn performed via a sequential quadratic programming (SQP) approach (Gill et al., 1981).

2.2. Identifiability criteria and singular value decomposition

Given a sample S of observations and a definition of the free parameters $\boldsymbol{p}$, it is important to assess the well posedness of problem (3). One useful tool for understanding the characteristics of a given identification problem is Cramér–Rao analysis (Jategaonkar, 2006; Klein and Morelli, 2006; Cramér, 1946), which gives a lower bound on the variance of the estimates. Indicating as $\overline{\boldsymbol{p}}$ the true (unknown) parameter values, the covariance of their estimates $\boldsymbol{p}^*$ is bound from below as

$$\mathrm{Var}(\overline{\boldsymbol{p}} - \boldsymbol{p}^*) \geq \boldsymbol{F}^{-1}, \tag{7}$$

where $\boldsymbol{F} \in \mathbb{R}^{n\times n}$ is the Fisher information matrix

$$\boldsymbol{F} = \sum_{i=1}^{N} \boldsymbol{G}_i^T \boldsymbol{R}^{-1}\boldsymbol{G}_i, \tag{8}$$

and $\boldsymbol{G}_i \in \mathbb{R}^{m\times n}$ the sensitivity of the ith observation of output vector $\boldsymbol{y}$ with respect to the parameters $\boldsymbol{p}$, i.e. $\boldsymbol{G}_i = \partial \boldsymbol{y}_i/\partial \boldsymbol{p}$. Criterion (7) can be used a priori, i.e. before having estimated the parameters, to understand the well-posedness of the problem, and a posteriori, i.e. after the solution of (3), to judge the accuracy of the computed result. Clearly, small values or linear dependencies in the sensitivity matrix $\boldsymbol{G}$ lead to a singular or nearly singular information matrix $\boldsymbol{F}$, and hence to large uncertainties in the estimates.

The collinearity between two parameters can also be assessed by the elements of the Fisher information matrix inverse. Denoting as $d_{p,q}$ the element of $\boldsymbol{F}^{-1}$ located at row p and column q, the correlation between the pth and qth parameters is computed as

$$\chi_{p,q} = \frac{d_{p,q}}{\sqrt{d_{p,p}d_{q,q}}}. \tag{9}$$

Low identifiability is indicated by high (typically >0.90) values of $\chi_{p,q}$, for $p \neq q$.

Although the Cramér–Rao inequality and the correlation matrix are important tools for the understanding of the well-posedness of an estimation problem and of the quality of the identified model, they still offer little help in practice in the case of difficult estimation problems. In fact, if an ill-posed case is detected, none of these quantities offers a constructive way of reformulating a better problem, and one is left to a trial and error approach in the often vane quest for an improved choice of parameters.

This situation can be ameliorated by the use of the SVD (Golub and van Loan, 1996). By this approach, the original problem expressed in terms of the physical parameters $\boldsymbol{p}$ is recast in terms of a new optimal set of statistically independent parameters. SVD-based identification in the context of robotics applications has been previously described in Sheu and Walker (1991), Shome et al. (1998), Khalil and Dombre (2002), and Waiboer (2007).

From its definition, the Fisher matrix can be factorized as

$$\boldsymbol{F} = \boldsymbol{M}^T\boldsymbol{M}, \tag{10}$$

where $\boldsymbol{M} \in \mathbb{R}^{Nm\times n}$ is defined as

$$\boldsymbol{M} = \begin{bmatrix} \boldsymbol{R}^{-1/2}\boldsymbol{G}_1 \\ \boldsymbol{R}^{-1/2}\boldsymbol{G}_2 \\ \vdots \\ \boldsymbol{R}^{-1/2}\boldsymbol{G}_N \end{bmatrix}. \tag{11}$$

In a typical identification problem $Nm \gg n$, as the number of measurements is much larger than the number of unknowns. The SVD of matrix $\boldsymbol{M}$ is

$$\boldsymbol{M} = \boldsymbol{U}\boldsymbol{\Sigma}\boldsymbol{V}^T, \tag{12}$$

where $\boldsymbol{U} \in \mathbb{R}^{Nm\times Nm}$ and $\boldsymbol{V} \in \mathbb{R}^{n\times n}$ are square orthogonal matrices, whose columns are respectively the left and right singular vectors of $\boldsymbol{M}$. Matrix $\boldsymbol{\Sigma} \in \mathbb{R}^{Nm\times n}$ is structured as

$$\boldsymbol{\Sigma} = \begin{bmatrix} \boldsymbol{S} \\ \boldsymbol{0} \end{bmatrix}, \tag{13}$$

where $\boldsymbol{S} \in \mathbb{R}^{n\times n}$ is a diagonal matrix whose entries s_i are the singular values, customarily sorted in descending order, i.e. $s_1 \geq s_2 \geq \cdots \geq s_n \geq 0$.

It is readily verified that, given Eq. (12), the information matrix is decomposed as

$$\boldsymbol{F} = \boldsymbol{V}\boldsymbol{S}^2\boldsymbol{V}^T, \tag{14}$$

where the columns of $\boldsymbol{V}$ can now be interpreted as the eigenvectors of $\boldsymbol{F}$, and s_i^2 as its eigenvalues. Similarly, the information matrix inverse is decomposed as $\boldsymbol{F}^{-1} = \boldsymbol{V}\boldsymbol{S}^{-2}\boldsymbol{V}^T$. This decomposition suggests a change of variables from the physical parameters $\boldsymbol{p}$ to a new set of unknowns:

$$\boldsymbol{\theta} = \boldsymbol{V}^T\boldsymbol{p}, \tag{15}$$

where $\boldsymbol{\theta}$ represents the new parameters obtained by rotation of $\boldsymbol{p}$ with the right singular vectors. Conversely, the original parameters

can be recovered from the new ones as $\boldsymbol{p}=\boldsymbol{V}\boldsymbol{\theta}$. Using (7), the Cramér–Rao bounds for the estimates $\boldsymbol{\theta}^*$ of the new unknown true values $\overline{\boldsymbol{\theta}}$ are

$$\mathrm{Var}(\overline{\boldsymbol{\theta}}-\boldsymbol{\theta}^*)\geq \boldsymbol{S}^{-2}. \tag{16}$$

Hence, the new parameters are statistically independent, being their covariance a diagonal matrix.

This decoupling significantly simplifies the identification design problem, as one can now select an acceptable threshold for the variance of the estimates and identify only those parameters that are associated with a lower Cramér–Rao bound, i.e. only those that can be estimated with a satisfactory level of accuracy.

This can be seen as follows. An unconstrained secant Newton solution (see Jategaonkar, 2006) of problem (3) for frozen covariance (step 1 of the iterative approach of Section 2.1) reads

$$\boldsymbol{F}\Delta\boldsymbol{p}=-\frac{\partial\hat{J}}{\partial\boldsymbol{p}}, \tag{17}$$

where $\Delta\boldsymbol{p}$ is the correction to the current value of the parameters. Using the SVD of the Fisher matrix, which is also the Jacobian of the problem, and recasting in terms of the $\boldsymbol{\theta}$ parameters, the problem is diagonalized and becomes

$$\boldsymbol{S}^2\Delta\boldsymbol{\theta}=-\boldsymbol{V}^T\frac{\partial\hat{J}}{\partial\boldsymbol{p}}. \tag{18}$$

It is clear that small singular values in $\boldsymbol{S}$ imply the near singularity of the Jacobian of the recast problem. From this point of view, setting now an acceptable threshold for the variance of the estimates means choosing a lower bound for the singular values, so as to ensure that the matrix is full rank and the problem solvable. To this end, matrix $\boldsymbol{S}$ can now be partitioned as

$$\boldsymbol{S}=\begin{bmatrix}\boldsymbol{S}_{\mathrm{ID}} & \boldsymbol{0}\\ \boldsymbol{0} & \boldsymbol{S}_{\mathrm{NID}}\end{bmatrix}, \tag{19}$$

where $\boldsymbol{S}_{\mathrm{ID}}$ contains all singular values such that $s_i\geq 1/\sigma_t$, σ_t^2 being the highest acceptable variance of the estimates, while $\boldsymbol{S}_{\mathrm{NID}}$ is approximated as

$$\boldsymbol{S}_{\mathrm{NID}}\approx\boldsymbol{0}. \tag{20}$$

The vector of parameters $\boldsymbol{\theta}$ and the matrix $\boldsymbol{V}$ of right singular vectors are accordingly partitioned as $\boldsymbol{\theta}=(\boldsymbol{\theta}_{\mathrm{ID}}^T,\boldsymbol{\theta}_{\mathrm{NID}}^T)^T$ and $\boldsymbol{V}=[\boldsymbol{V}_{\mathrm{ID}}\boldsymbol{V}_{\mathrm{NID}}]$, and the estimation problem (3) is now solved in terms of the sole identifiable parameters, i.e. using

$$\boldsymbol{p}\approx\boldsymbol{V}_{\mathrm{ID}}\boldsymbol{\theta}_{\mathrm{ID}}. \tag{21}$$

Finally, the left singular vectors can be used for understanding the contribution of each single observation $\boldsymbol{y}_i$ to the estimation of the new parameters. In fact, by partitioning the left singular vector matrix in row blocks as

$$\boldsymbol{U}=\begin{bmatrix}\boldsymbol{U}_1\\ \boldsymbol{U}_2\\ \vdots\\ \boldsymbol{U}_N\end{bmatrix}, \tag{22}$$

one can readily show that the gradients of the outputs with respect to $\boldsymbol{\theta}$ are

$$\frac{\partial\boldsymbol{y}_i}{\partial\boldsymbol{\theta}}=\boldsymbol{R}^{1/2}\boldsymbol{U}_i\boldsymbol{\Sigma}. \tag{23}$$

2.3. Definition of estimation parameters

A lifting line within a BEM approach describes a blade in terms of airfoils, specifying their spanwise twist and chord distributions, as well as their aerodynamic center location with respect to a reference line. For each airfoil, aerodynamic properties are given in terms of lift C_L, drag C_D and possibly moment C_M coefficients vs. angle of attack α, possibly parameterized in terms of the Reynolds number. Such quantities are typically obtained by wind tunnel tests or numerical simulations, and stored in look-up table form. Hence, the aerodynamic properties of a lifting line can be thought of as functions of the angle of attack α and of the spanwise blade location η, with $\eta=0$ at the blade root and $\eta=1$ at the tip.

In this work, the physical quantities used for model parameterization are defined as unknown additive functions that correct some available (baseline) airfoil quantities. For the kth aerodynamic property C_k ($k=L$ for lift, or $k=D$ for drag), this correction is expressed as

$$C_k(\alpha,\eta)=C_k^0(\alpha,\eta)+\Delta_k(\alpha,\eta), \tag{24}$$

where $C_k^0(\alpha,\eta)$ is the baseline quantity, while $\Delta_k(\alpha,\eta)$ is the additive corrective function. In turn, each corrective function is discretized by the following two-dimensional interpolation over the α–η domain:

$$\Delta_k(\alpha,\eta)=\boldsymbol{n}^T(\alpha,\eta)\boldsymbol{p}_k, \tag{25}$$

where $\boldsymbol{n}(\alpha,\eta)$ is a vector of two-dimensional shape functions and $\boldsymbol{p}_k$ the vector of associated nodal values of the interpolation for the kth property. In this work, simple bilinear shape functions were used, although other choices are clearly possible. Finally, the vector of physical property parameters is defined as $\boldsymbol{p}=(\boldsymbol{p}_L^T,\boldsymbol{p}_D^T)^T$, stacking the lift and drag nodal parameter vectors. To maintain the aerodynamic properties within acceptable physical values, suitable bounds can be enforced as inequality constraints within the optimization process. Noting respectively $\boldsymbol{l}_{\mathrm{par}}$ and $\boldsymbol{u}_{\mathrm{par}}$ the upper and lower parameter bounds, such constraints are simply formulated as $\boldsymbol{l}_{\mathrm{par}}\leq\boldsymbol{p}\leq\boldsymbol{u}_{\mathrm{par}}$. In the present work, bounds were used to express the necessary positivity of drag, although the corresponding inequalities were never active at convergence.

With the SVD approach, the change of variables $\boldsymbol{p}=\boldsymbol{V}_{\mathrm{ID}}\boldsymbol{\theta}_{\mathrm{ID}}$ is used; here the partitioning of the parameter vector $\boldsymbol{p}$ in the lift and drag parts induces a similar row-block partitioning of the right singular vector matrix. In terms of the new set of parameters, the interpolation of the corrective function over the α–η domain becomes

$$\Delta_k(\alpha,\eta)=\boldsymbol{\psi}_k^T(\alpha,\eta)\boldsymbol{\theta}_{\mathrm{ID}}, \tag{26}$$

where $\boldsymbol{\psi}_k(\alpha,\eta)=\boldsymbol{V}_{\mathrm{ID}_k}^T\boldsymbol{n}(\alpha,\eta)$ is the vector of eigenshapes of the aerodynamic corrections, and $\boldsymbol{V}_{\mathrm{ID}_k}$ is the row block corresponding to either lift or drag. Through $\boldsymbol{\psi}_k$, the identifiable parameters have now an effect on both lift and drag, coupling them together, coherently with the coupled nature of the problem. Moreover, a visual inspection of the eigenshape functions helps in clarifying the actual identifiability of physical parameters in the various regions of the domain, and this contributes to the overall understanding of the characteristics of the estimation problem. Possible bounds on the parameters are also affected by the change of variable, and are readily expressed as

$$\boldsymbol{l}_{\mathrm{par}}\leq\boldsymbol{V}_{\mathrm{ID}}\boldsymbol{\theta}_{\mathrm{ID}}\leq\boldsymbol{u}_{\mathrm{par}}. \tag{27}$$

Due to the intrinsic nonlinearity of the problem, the sensitivity matrices $\boldsymbol{G}_i$ as well as the residual covariance $\boldsymbol{R}$ depend on the free parameters; in turn, this means that the SVD results change when the parameters change. On account of this, the SVD eigenshape functions should be updated, and this can be done within the Newton iterations of problem (3) or within the major iterations of the algorithm of Section 2.1; the latter approach was followed in the present work.

2.4. Definition of outputs

In this work the problem outputs $\boldsymbol{y}$ associated to the experimental observations $\boldsymbol{z}$ are defined as

$$\boldsymbol{y} = (C_P, C_F, \ldots, C^j_{Mx}, C^j_{My}, \ldots)^T, \quad j = 1, N_{\text{sec}}. \tag{28}$$

C_P and C_F are respectively the rotor power and thrust coefficients defined as

$$C_P = \frac{P}{1/2\rho V^3 A}, \tag{29a}$$

$$C_F = \frac{F}{1/2\rho V^2 A}, \tag{29b}$$

where P is power, F is thrust, ρ the air density, V the wind speed, $A = \pi R^2$ the rotor area and R its radius. C_P and C_F, in turn, depend on blade pitch β and on the tip speed ratio (TSR) $\lambda = \Omega R/V$. Similarly C^j_{Mx} and C^j_{My} are non-dimensional moment coefficients related to the in and out-of-plane bending moments M_x and M_y at the generic jth blade cross section, coefficients that are defined as

$$C^j_{Mx,y} = \frac{M^j_{x,y}}{1/2\rho V^2 A R}, \tag{30}$$

while N_{sec} is the number of blade sections where such quantities are measured.

Even in stationary winds, the operating conditions of wind turbines are non-stationary because of non-uniform and non-axial inflow over the rotor disk. For this reason, measurements $\boldsymbol{z}$ associated to the outputs $\boldsymbol{y}$ defined above have to be intended as obtained by averaging over a suitable number of rotor revolutions.

3. Results

3.1. Calibration of the lifting line model of a scaled rotor

3.1.1. Description of experimental measurements

The proposed approach was used for the calibration of the lift and drag characteristics of the rotor of an aeroelastically scaled and actively controlled wind turbine model, described in more detail in Bottasso et al. (2013b).

The rotor has a diameter of 2 m, with a solidity of about 0.04. To account for the rather small chord-based Reynolds due to the reduced size of the model, the blade was designed using the special low-Reynolds airfoils AH79-100C (Althaus, 1988) and WM006 (Olesen, 2009), the former airfoil being used in the inboard section of the blade and the latter in the outboard one. Not to alter the aerodynamic characteristics of the airfoils, interpolations of the cross sectional shapes were limited to a relatively small transition region between the inboard and outboard sections, and at the root region to smoothly deform the inboard airfoil

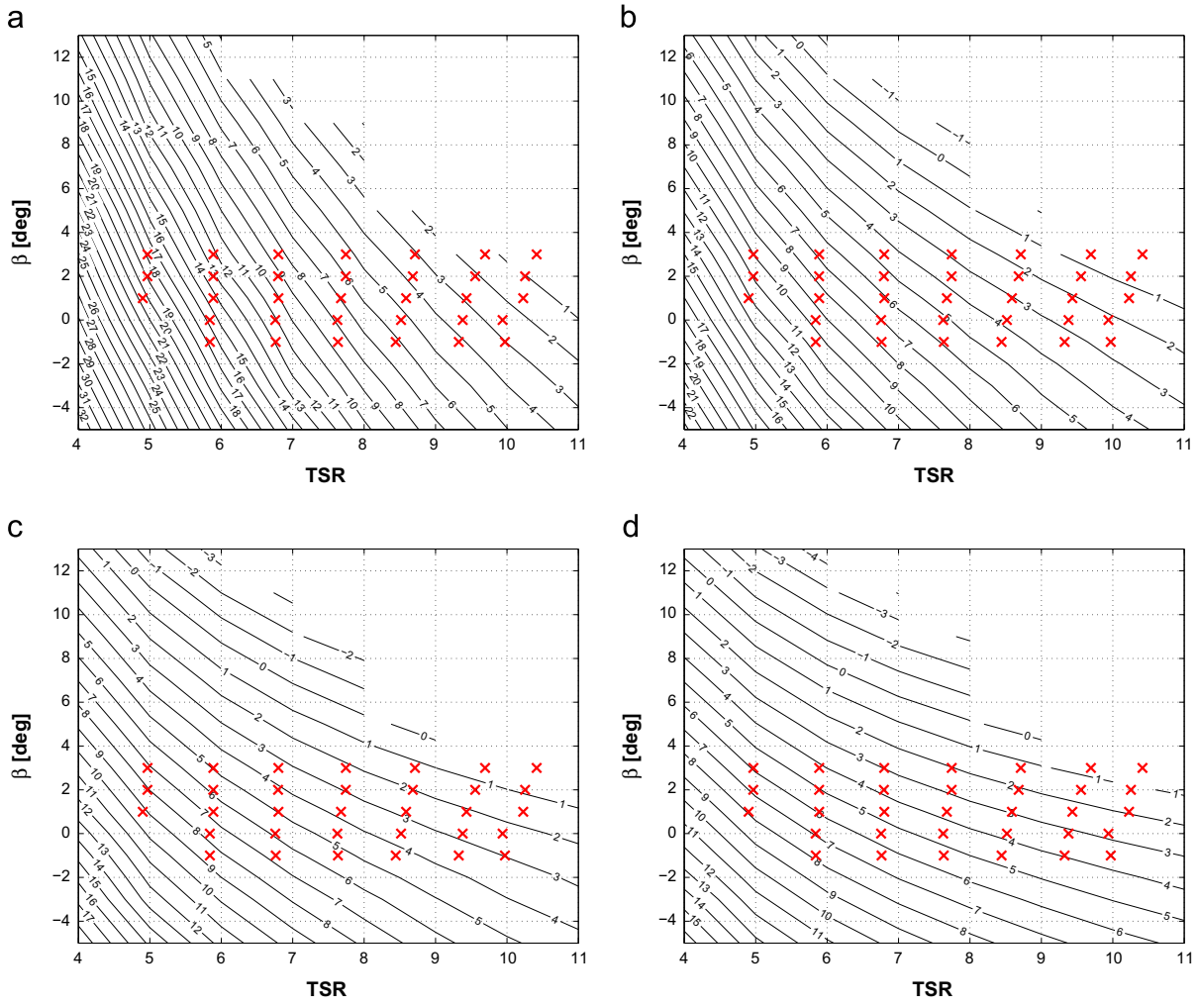

Fig. 3. Angles of attack at different blade spanwise locations for the various testing conditions (' × ' marks). (a) Angles of attack of AH79-100C at $\eta = 0.14$. (b) Angles of attack of AH79-100C at $\eta = 0.42$. (c) Angles of attack of WM006 at $\eta = 0.70$. (d) Angles of attack of WM006 at $\eta = 0.95$.

into the blade root cylinder. The blade spanwise chord distribution was geometrically scaled from the one of a reference full-scale machine; on the other hand, to account for the change of airfoils between full scale and scaled blades, the blade twist was modified to yield an optimal spanwise distribution of the axial induction factor. The blades were equipped with transition strips, with variable chordwise width and spanwise thickness, that were optimized with the goal of maximizing aerodynamic power.

A high fidelity multibody model of the wind turbine was developed by means of the aeroservoelastic simulation code `Cp-Lambda`, based on a finite element multibody approach (Bauchau et al., 2001; Bottasso and Croce, 2006–2013). The rotor blades are modeled by geometrically exact beam elements, whose stiffness and mass properties were previously validated by means of modal frequency measurements (Bottasso et al., 2013b). The aerodynamics is modeled by means of the blade-element momentum (BEM) model, based on the annular stream-tube theory with wake swirl.

Rotor torque was measured by means of strain gages located on the shaft, and previously calibrated by using known dead weights, while rotor speed was obtained by an optical encoder. The longitudinal force generated by the turbine was measured by a balance located at the tower base. The balance reading was corrected for rotor up-tilt and by subtracting the drag of the tower-nacelle assembly, as measured in separate tests conducted on the turbine without the blades, yielding the rotor thrust. The unperturbed wind speed was measured upwind of the wind turbine by a triple hot wire probe, while air density was computed from the recorded air pressure, temperature and humidity. The measured thrust and power data, as well as the TSR, were corrected for blockage by applying the disk actuator method proposed in Bahaj et al. (2007) and verified by RANS CFD simulations of the experiment with and without wind tunnel walls.

Rotor aerodynamic performance was measured by testing the model in the low-turbulence aeronautical test section of the wind tunnel at the Politecnico di Milano, for varying wind speed, rotor speed and blade pitch settings. Testing conditions were optimized to cover a wide range of angles of attack, while at the same time keeping the Reynolds number as high as possible and similar across the various test points. Fig. 3 shows contour plots of the angles of attack at four spanwise stations for varying blade pitch angle β and TSR. In the graphs, '$\times$' symbols mark the testing conditions where measurements of rotor performance were obtained. It appears that the angle of attack range for the AH79-100C airfoil is about $[-1$ to $20]$ deg, covering the pre-stall, stall and post-stall regimes; on the other hand, the range for WM006 is circa [0–10] deg, and limited to the pre-stall regime.

Not insignificant differences were observed between the experimentally measured and theoretical BEM-based rotor aerodynamic performance, computed using the nominal airfoil polars obtained by other authors from wind tunnel measurements. The small size of the blade prevented the direct local measurement of airfoil aerodynamic characteristics by pressure taps or other means. Hence, the procedure described in this work was applied to infer the airfoil characteristics from the experimental measurements of the global rotor performance, this way bypassing the need for realizing difficult local measurements.

3.1.2. *Direct identification of physical parameters*

At first, the identification of the aerodynamic properties of the airfoils was attempted by using the physical parameters $\boldsymbol{p}$, i.e. the nodes of the α–η interpolation of the corrective functions defined in Eq. (25). Linear shape functions in the α range were used, with nodes located at -1, 4, 8, 11 and 14 deg for the AH79-100C airfoil, and at 1, 4, 7, 10 deg for the WM006 one. In the η range, constant shape functions were used in the spanwise sections where the two airfoils are used, and linear ones for the transition segment.

Fig. 4 shows the power coefficients vs. TSR for various blade pitch settings. Triangle symbols mark the experimental

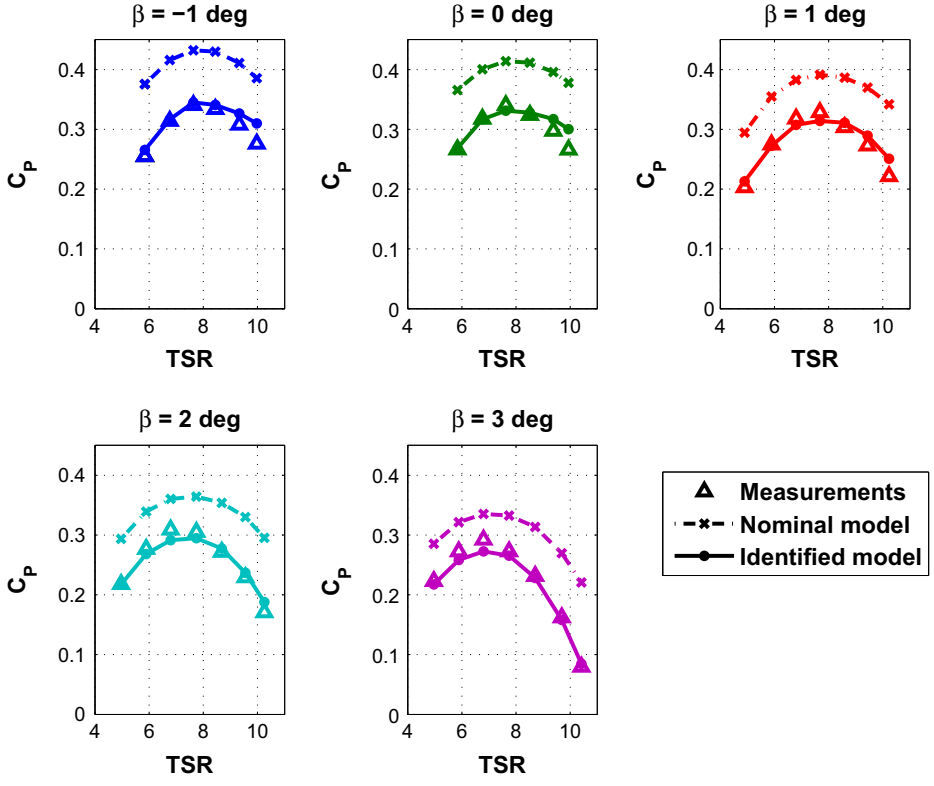

Fig. 4. Power coefficients C_P vs. TSR for various blade pitch settings β by the direct identification of aerodynamic parameters. Triangles: experimental measurements; dashed lines: BEM model prior to identification; solid lines: identified BEM model.

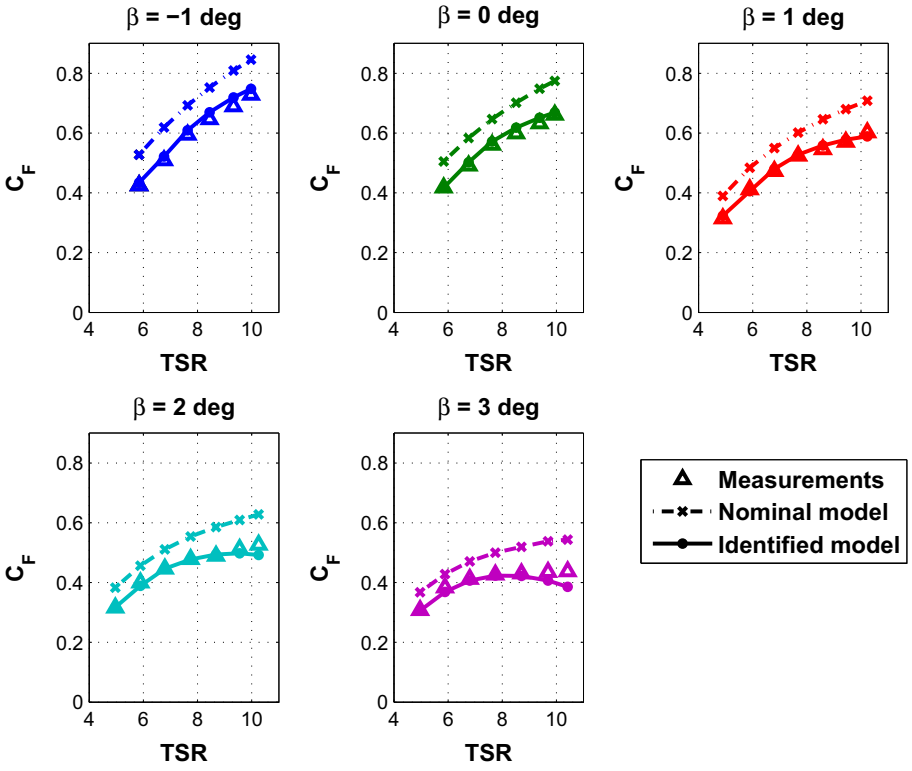

Fig. 5. Thrust coefficients C_F vs. TSR for various blade pitch settings β by the direct identification of aerodynamic parameters. Triangles: experimental measurements; dashed lines: BEM model prior to identification; solid lines: identified BEM model.

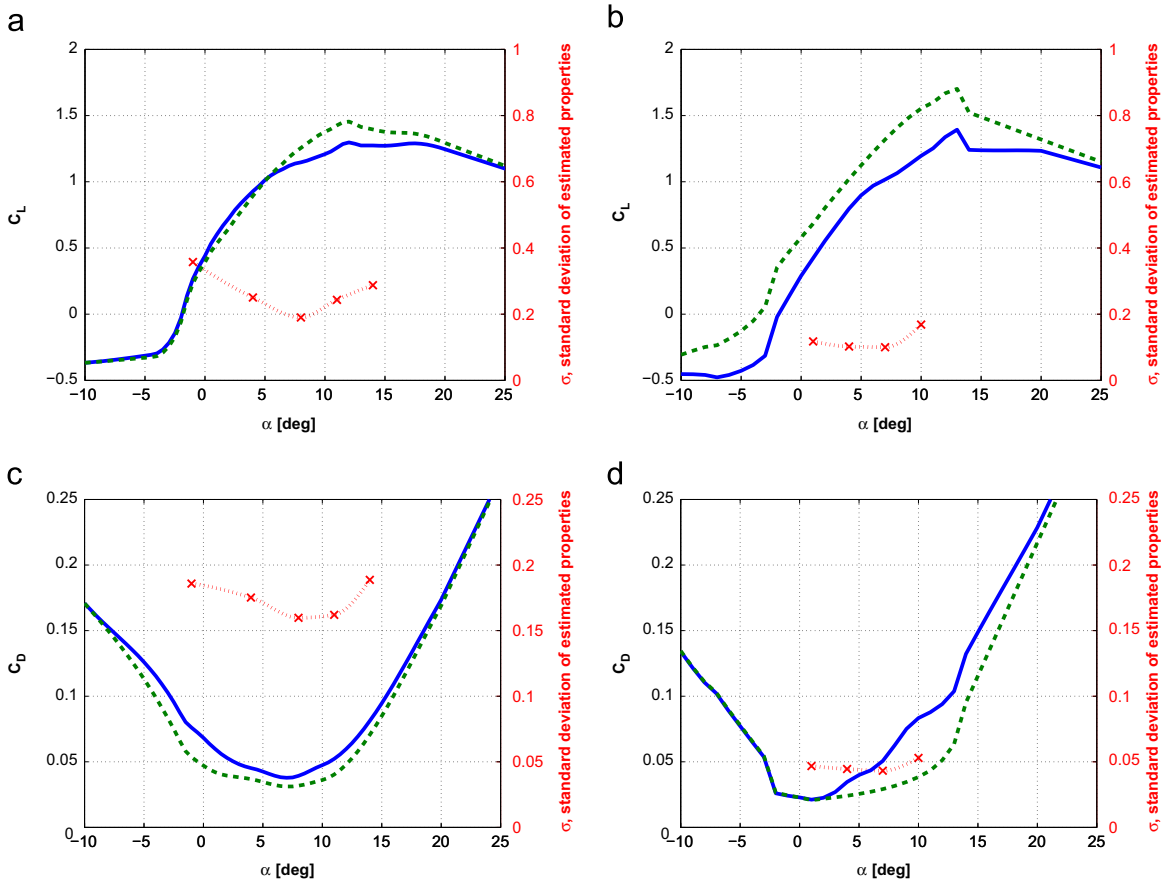

Fig. 6. Lift and drag coefficients vs. angle of attack for the two airfoils. Nominal values: dashed lines; identified model: solid lines; Cramér–Rao standard deviations: dotted lines. (a) Lift coefficient of AH79-100C. (b) Lift coefficient of WM006. (c) Drag coefficient of AH79-100C. (d) Drag coefficient of WM006.

measurements; dashed lines indicate the output of the BEM model using the nominal aerodynamic properties, i.e. prior to identification, while solid lines report the results after identification. Similarly, Fig. 5 shows the thrust coefficients. There are large discrepancies between the outputs of the nominal model and the measurements. Assuming that the BEM model is capable of realistically representing the aerodynamics of the rotor in this nearly axial and very nearly steady condition, which is quite likely, it is reasonable to assume that these discrepancies can be traced back to the airfoils not behaving as predicted by their nominal aerodynamic characteristics. On the other hand, the match after identification appears to be much improved.

Fig. 6 reports the lift and drag coefficients of the two airfoils plotted vs. the angle of attack. Each figure shows the nominal characteristics using a dashed line, the identified properties using a solid line, and finally the Cramér–Rao standard deviation of the estimates using a dotted line. The lift coefficients of the WM006 airfoil appear to be very different from the nominal ones: the identified lift curve appears to be shifted downwards as the airfoil had a lower camber. Due to the reduced dimensions of the blade, even small imprecisions in the blade manufacturing process could cause considerable dissimilarities in the shape of the airfoils, in turn leading to large differences in the aerodynamic properties. The standard deviation of the estimates for the inner, AH79-100C, and outer, WM006, airfoils are quite different. In particular, the outer airfoil has a much higher level of confidence than the inner one. This is expected, as the outer part of the blade plays a major role in determining the rotor characteristics.

Analysis of the correlation matrix shows a strong collinearity among the airfoil property parameters, as seen in Table 1 for the lift coefficients. In particular, it appears that the lift of the inner airfoil is highly correlated to the lift of the outer one in the pre-stall range. Similar results and conclusions are obtained by looking at the correlation of the drag coefficients.

Although the quality of the identification, as seen by looking at the global rotor performance, appears deceptively good, these simple considerations highlight the difficulty of the problem. First, the sensitivity of the outputs with respect to the inner airfoil parameters is low. As a consequence, estimates of the inner airfoil properties have a very low level of confidence. Furthermore, there is a high level of correlation between inner and outer airfoils. Therefore, any error in the identification of the former affects in a significant and unpredictable way estimates of the latter. These problems clearly illustrate the limits of the approach based on the direct identification of the physical properties.

3.1.3. *SVD-based identification*

The SVD-based approach was used for repeating the identification, using the same experimental data of the previous section. Bilinear shape functions were employed in this case, with nodes located at $\alpha = -8, 1, 3, 5, 7, 9, 25$ deg and at $\eta = 0, 0.2, 0.4, 0.6, 0.8, 1.0$.

Table 1
Correlation matrix of the lift parameters.

Nodes [deg]	AH79-100C					WM006			
	−1	4	8	11	14	1	4	7	10
AH79-100C									
−1	1.00	0.88	0.76	0.63	0.45	**−0.98**	−0.89	−0.75	−0.47
4	–	1.00	0.85	0.70	0.49	−0.92	**−0.99**	−0.82	−0.50
8	–	–	1.00	0.76	0.52	−0.78	−0.86	**−0.95**	−0.47
11	–	–	–	1.00	0.53	−0.65	−0.70	−0.85	−0.72
14	–	–	–	–	1.00	−0.45	−0.50	−0.56	−0.85
WM006									
1	–	–	–	–	–	1.00	**0.93**	0.78	0.48
4	–	–	–	–	–	–	1.00	0.83	0.51
7	–	–	–	–	–	–	–	1.00	0.56
10	–	–	–	–	–	–	–	–	1.00

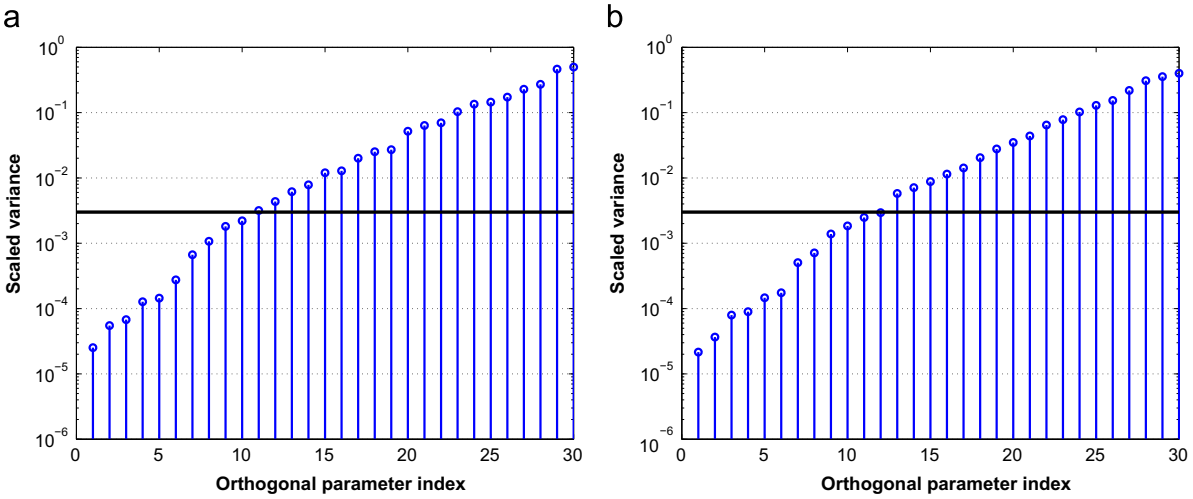

Fig. 7. Variance of the orthogonal parameters based on the nominal model (at left) and after a first estimation (at right). The black horizontal solid line indicates the identifiability threshold. (a) Based on nominal model. (b) After first estimation.

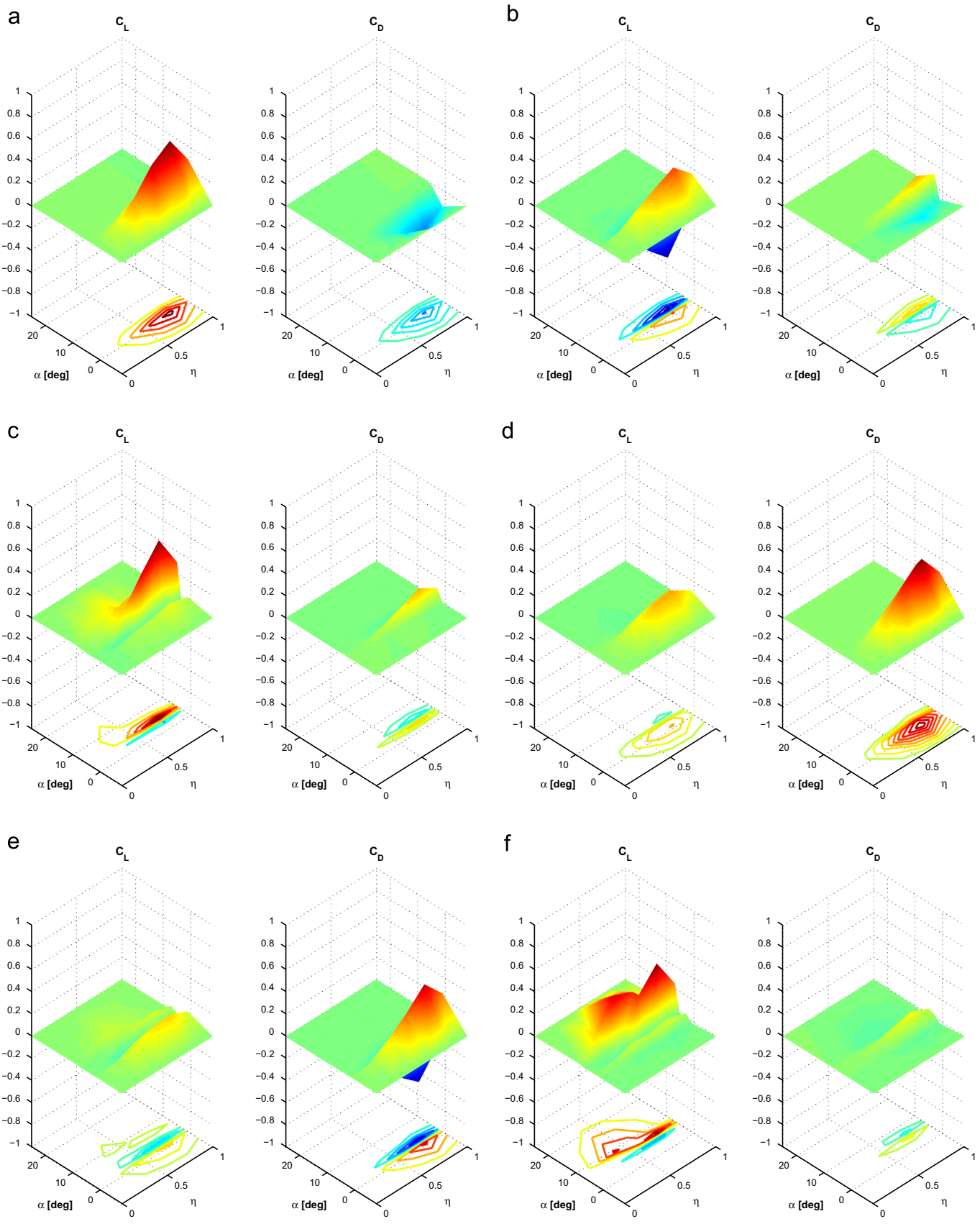

Fig. 8. The lowest six identifiable eigenshapes. (a) 1st eigenshape. (b) 2nd eigenshape. (c) 3rd eigenshape. (d) 4th eigenshape. (e) 5th eigenshape. (f) 6th eigenshape.

Based on the nominal model, a first analysis of the singular values was attempted. The sensitivities of the outputs with respect to the scaled physical parameters were computed by finite differences, while the noise covariance was assumed to be $\boldsymbol{R} = \sigma_e^2 \boldsymbol{I}$, with $\sigma_e = 0.005$, which is a reasonable value for both C_P and C_F.

At left, Fig. 7(a) shows the variance of the orthogonal parameters, $\sigma^2_{\theta_i} = 1/s_i^2$, computed for the nominal model, i.e. prior to any estimation. The identifiability threshold, also shown in the plot as a horizontal solid line, was chosen equal to 0.003, which corresponds to an expected standard deviation of the identified parameters of about 5.5% of their reference values. The plot illustrates the fact that there are only 10 parameters that are actually identifiable with a good level of accuracy.

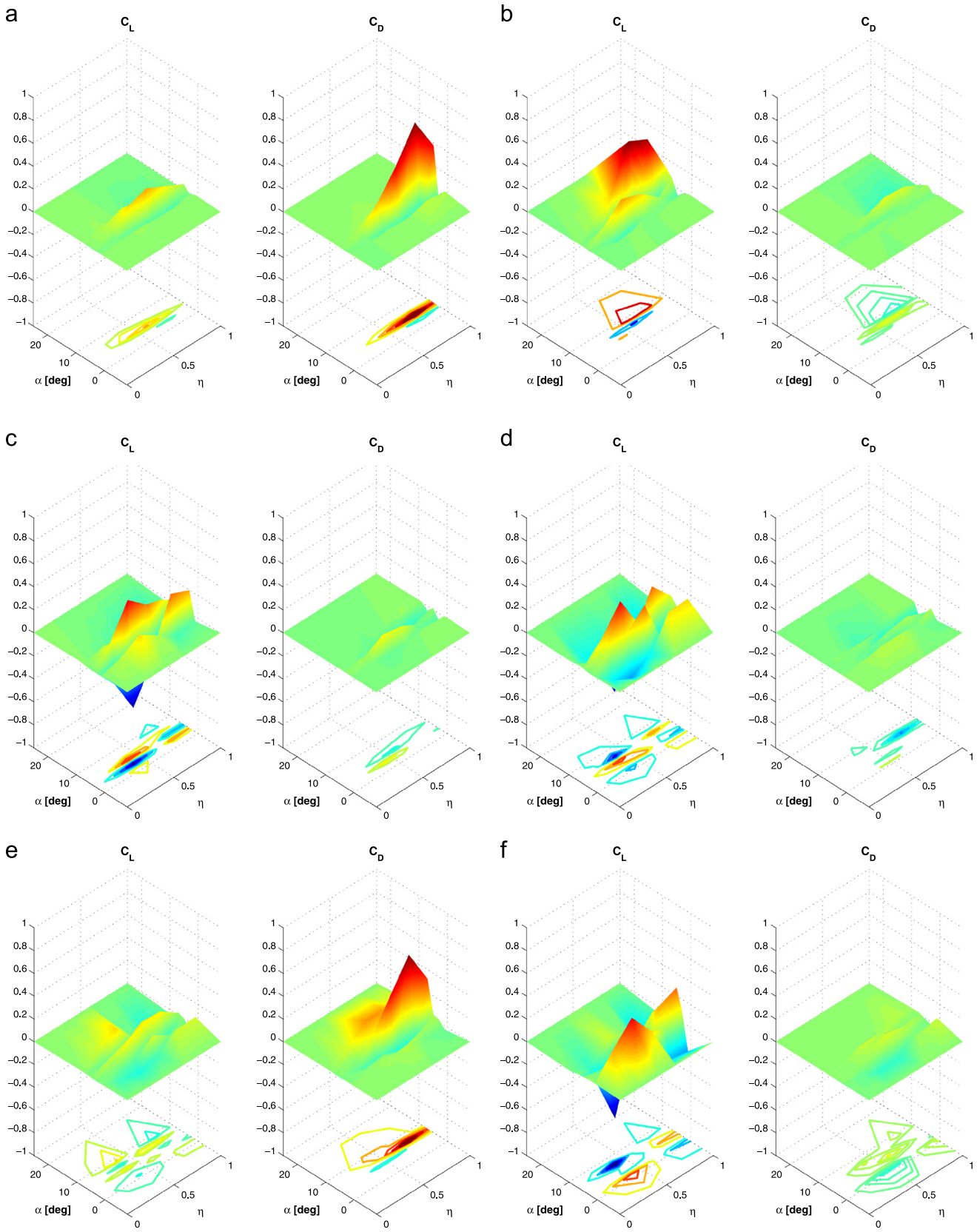

Fig. 9. The next six lowest identifiable eigenshapes. (a) 7th eigenshape. (b) 8th eigenshape. (c) 9th eigenshape. (d) 10th eigenshape. (e) 11th eigenshape. (f) 12th eigenshape.

After having performed a first estimation using the 10 identifiable orthogonal parameters, the SVD eigenshapes were updated recomputing the output sensitivity matrices and a second optimization was performed. The updated variance of the orthogonal parameters is shown in Fig. 7(b) at right. The number of identifiable parameters is now equal to 12, a slight increase with respect to the first estimate. Notice however that, by using the SVD to optimize the choice of unknowns, the number of free variables is now reduced with respect to the direct approach, where 18 parameters were used.

Figs. 8 and 9 show the SVD eigenshapes of the identifiable parameters. Visual inspection of these shape functions suggests the following comments:

- Due to the coupled nature of the problem, each shape is associated to both airfoil lift and drag.
- As expected, the root region, up to about 20% span, is characterized by little identifiability of the airfoil characteristics, drag being particularly poorly visible.
- Most shapes have 'crests' aligned with the η-axis. The sharp variations in the α direction highlight the ability of the various shapes in distinguishing the effects generated at different angles of attack. On the other hand, the typically more modest changes in the η direction show that it is harder to separate the effects of the various spanwise sections of the blade to a good level of confidence. This is to be expected, since only hub loads are used here, and it becomes therefore hard to distinguish the influence of the inboard and outboard airfoils. To have a better spanwise identifiability one needs to separate the effects of the various blade regions by using spanwise load measurements, as illustrated later on.
- The lowest three eigenshapes are mostly associated to lift in the outer blade segment, which was in fact found to be the most identifiable quantity using the direct approach.

All these observations are in line with the limits that were found in the use of the direct approach.

Figs. 10 and 11 show the power and trust coefficients vs. TSR for different blade pitch settings, prior to and after identification. All plots show an excellent correlation of the calibrated model with the measurements. Even if a slight underestimation of the C_P coefficient for pitch angles of 2 and 3 deg still remains, the correlation of this set of parameters is better than the one obtained by the direct approach.

For the blade section located at $\eta=0.86$, Fig. 12 shows the lift (at left) and drag (at right) vs. angle of attack α. The plots report the nominal (dashed line) and the identified (solid line) characteristics, as well as their standard deviations (dotted line); the direct identification results of the previous section are plotted using a thin solid line. Despite its limits, in this blade portion of high identifiability the direct approach achieves results that are apparently quite similar to the ones of the SVD-based approach. Notice however that the deviations of the lift and drag properties obtained by the SVD-based approach are respectively about one-half and one-fifth of those achieved with the direct method, and the estimates therefore now have a much improved level of confidence.

3.2. *Simulation study on the effects of multiple spanwise load measurements*

The experimental tests described in the previous section have shown that the calibration of the lifting line model of a rotor can be performed by using hub loads, and very noticeable improvements in the accuracy of the computed rotor power and thrust were reported even in the presence of a significant initial mismatch of the nominal model. Nonetheless, the analysis has also shown that the use of the sole hub loads has a somewhat limited ability in distinguishing the effects of multiple spanwise locations along the blade, which is indeed something to be expected

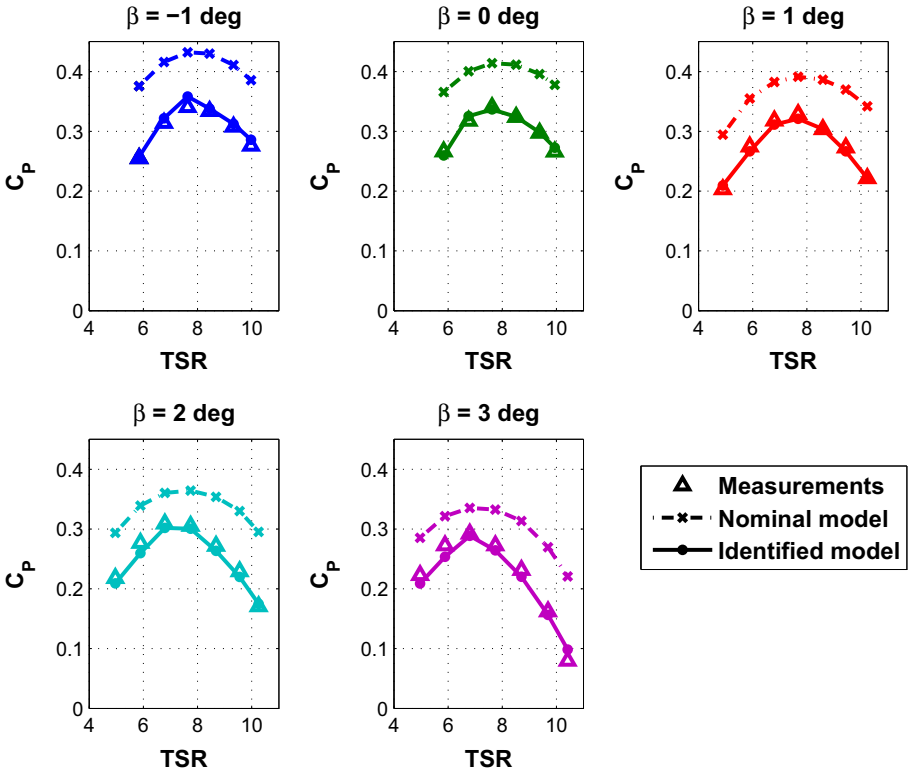

Fig. 10. Power coefficients C_P vs. TSR for various blade pitch settings β by the SVD-based identification of aerodynamic parameters. Triangles: experimental measurements; dashed lines: BEM model prior to identification; solid lines: identified BEM model.

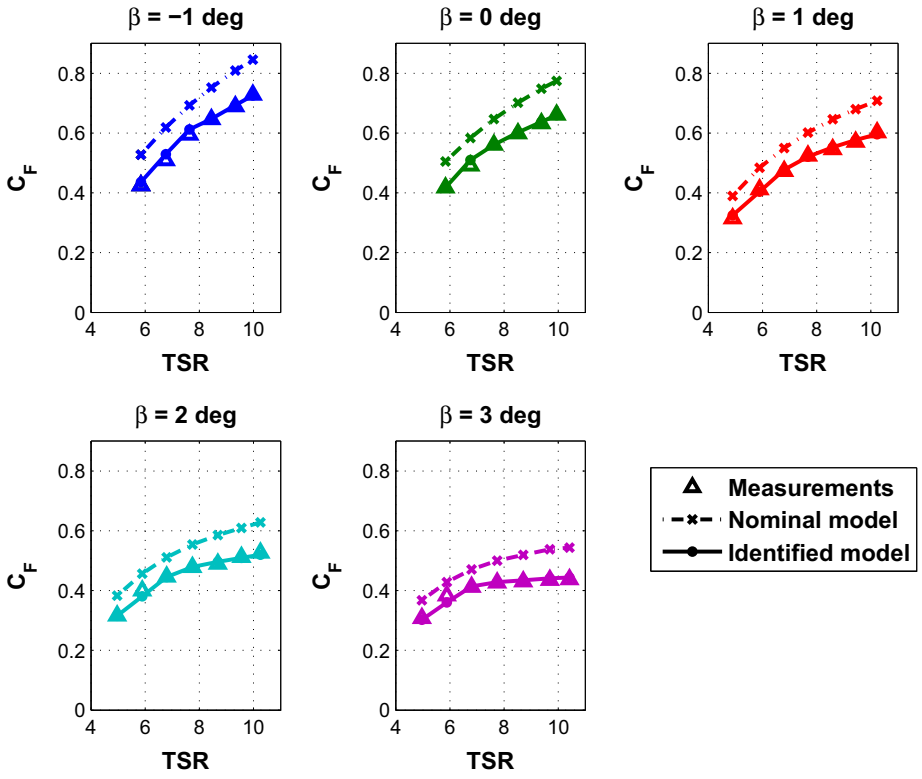

Fig. 11. Thrust coefficients C_F vs. TSR for various blade pitch settings β by the SVD-based identification of aerodynamic parameters. Triangles: experimental measurements; dashed lines: BEM model prior to identification; solid lines: identified BEM model.

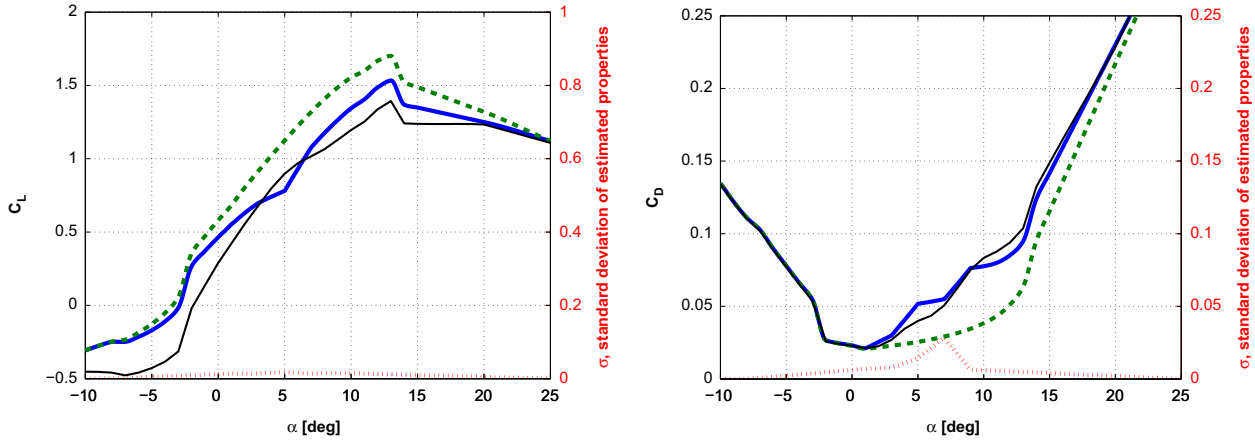

Fig. 12. Lift C_L and drag C_D coefficients vs. angle of attack α for the airfoil located at η=0.86. Thick solid lines: SVD-based identification; thin solid lines: direct approach; dashed lines: nominal properties; dotted lines: standard deviation of SVD-based estimates.

according to intuition. This fact has also been well illustrated by the inspection of the eigenshape functions that map the SVD parameters into the physical ones.

To clarify the effect that additional blade load measurements might have on the spanwise resolution of the method, a simulation study was conducted by using the same rotor model and choice of all parameters while increasing the number of sectional outputs N_{sec} in Eq. (28). The first sectional output was always located at the blade root, while the other ones were uniformly distributed along the blade span; in all cases, hub power and thrust were always included in the output vector.

Fig. 13 shows a sample of eigenshapes for $N_{sec}=1$ (blade root loads), $N_{sec}=2$ (blade root and mid-span loads), and $N_{sec}=3$ (blade root, one and two thirds span loads). Not all lowest identifiable eigenshapes are shown for space limitations, but this small sample is sufficient to illustrate the effects of addition measurements. For these three configurations, the number of identifiable parameters was 13, 17 and 18, with a progressive increase with respect to the 12 identifiable parameters when the sole hub loads were used. Visual inspection of the eigenshapes clearly shows an increased spanwise variability of the functions, with a consequent improved spanwise localization and resolution.

Fig. 13(a) and (b) shows eigenshapes that appear to be very similar to those of Figs. 8(a) and 9(c). Hence, it appears that the sole addition of blade root loads does not significantly improve on the situation with respect to the use of hub loads; this is to be expected, as the two sets of loads carry essentially the same informational content. On the other hand, the addition of measurement points along the blade span allows

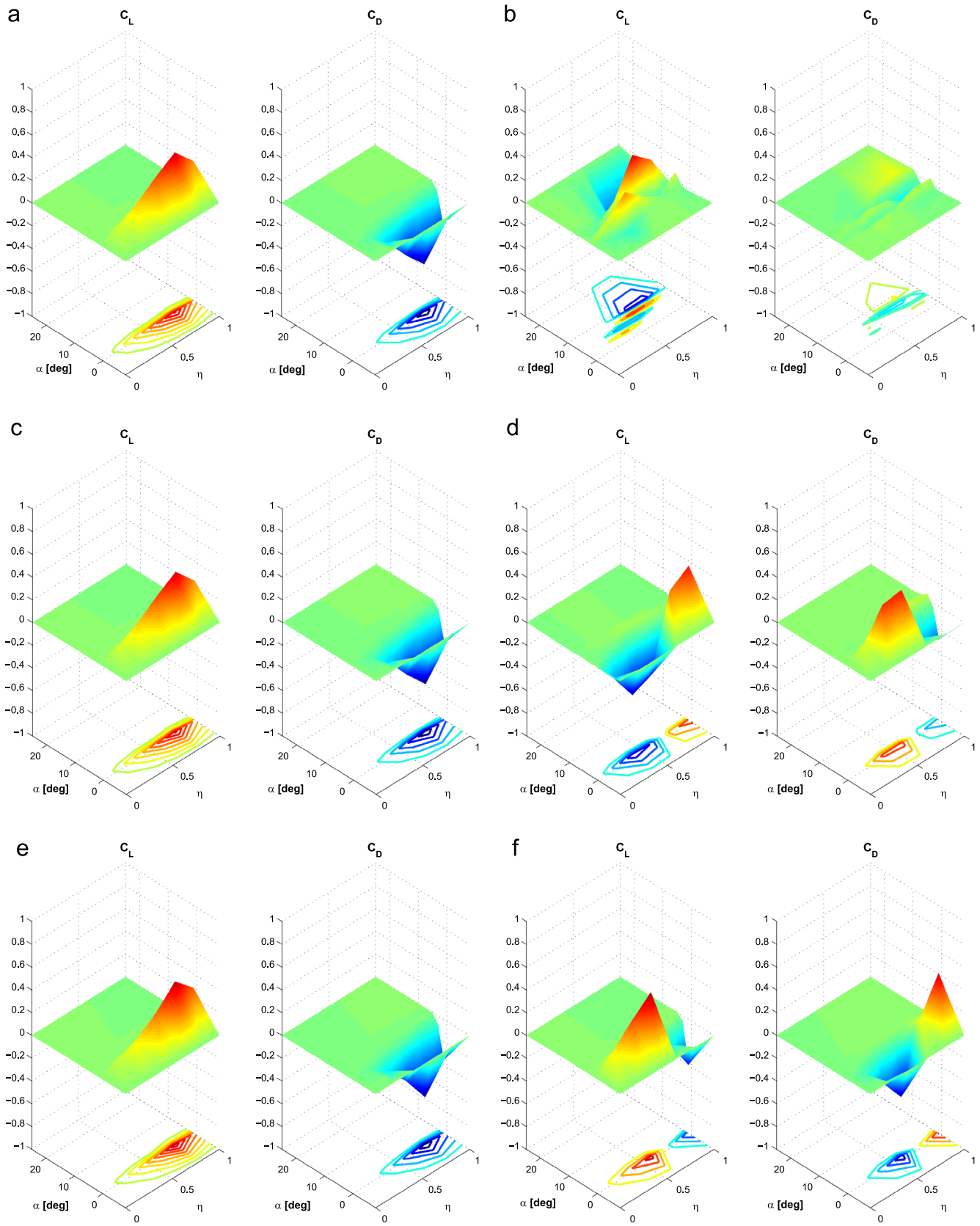

Fig. 13. Sample of identifiable eigenshapes for various spanwise blade load measurement configurations. (a) $N_{sec} = 1$, 1st eigenshape. (b) $N_{sec} = 1$, 8th eigenshape. (c) $N_{sec} = 2$, 1st eigenshape. (d) $N_{sec} = 2$, 8th eigenshape. (e) $N_{sec} = 3$, 1st eigenshape. (f) $N_{sec} = 3$, 7th eigenshape.

for a better separation of the effects of the various spanwise sections of the blade. As shown in Fig. 13(d) and (f), in this case sharp variations along the η-axis are present in the eigenshapes. It is also interesting to note, looking at Fig. 13(a), (c) and (e), that the first eigenshape is not significantly affected by the number of spanwise blade load measurements.

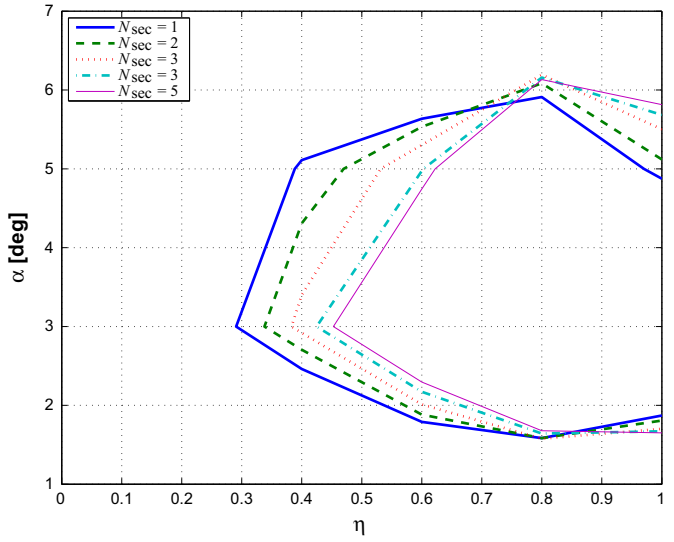

Fig. 14. Shrinking domain of influence of the second eigenshape for an increasing number of spanwise blade load measurement points.

Clearly, the larger the number of spanwise measurements, the better the spanwise localization becomes. This is illustrated in Fig. 14, which shows for the second eigenshape how the domain of influence, i.e. that region where the eigenshape differs from zero, is reduced as N_{sec} increases, indicating a sharper localization. It should be remarked that the optimal number and configuration of measurement points must in general be determined based on the specific goals and characteristics of any given application. In fact, while in numerical applications one can straightforwardly place measurement points anywhere along the blade, the situation is different when measuring actual blade loads, where the need for spanwise resolution must be traded against cost and complexity of installation.

4. Conclusions

This paper has considered the calibration of wind turbine lifting line models, to be used for a variety of possible simulations ranging from performance, to aeroelasticity, to CFD.

The problem has been formulated as a constrained optimization of a maximum likelihood cost function, that accounts for the presence of sensor and process noise, using rotor loads as driving measurements. The to-be-identified physical parameters have been selected as additive corrective functions of the airfoil lift and drag characteristics, interpolated with respect to angle of attack and blade span using suitable shape functions.

The direct identification of such physical parameters has been shown to be particularly difficult, due to low observability and collinearity, especially in the root region of the blade. To overcome this problem, easying and robustifying the calibration process, a novel SVD-based identification has been described. The approach makes use of the SVD of the square root of the Fisher information matrix, this way defining a new set of statistically independent identification parameters. By recasting the problem in terms of the new parameters, one can straightforwardly restrict the estimation to only those quantities that have sufficiently low variance, and hence that are reasonably observable given the available measurements. The associated eigenshapes map the same parameters back to the physical ones, a fact that can be used to gain a better understanding of the problem characteristics. Moreover, the SVD-based identification relieves the user from the burden of choosing the optimization parameters, a process often based on trial and error.

The main features of the formulation have been illustrated by means of examples, which allow for the following conclusions to be drawn. First, the sole use of hub loads was sufficient for obtaining a substantial improvement of the lifting line model of a scaled rotor, where the airfoils appeared to behave quite differently from their nominal expected characteristics. Clearly, improvements can be obtained only for conditions in the range of the available measurements, which should therefore cover the extension of angles of attack of interest. Second, drag, being much smaller than lift, has typically low observability, especially in the root region of the blade. Third, although reasonable results can be obtained by the sole use of hub loads, a more precise distinction among the effects of various spanwise sections requires multiple spanwise load measurements.

Conceptually, there is no reason why the new proposed method should not be usable also for the calibration of lifting line models from field test data on a machine that is equipped with the necessary sensors, although there are at least a couple of hurdles that would need to be overcome. First, one needs to sufficiently cover the range of angles of attack of interest, and this would require the machine to be operated at varying partialized set points. Second, the method as used here assumes steady or nearly steady operating conditions, which are nonexistent in practice because of wind variability and turbulence. One could compute suitable averages over properly chosen time windows, which would need some careful data processing, or one could also use a transient model instead of the present steady one, which however would also incur in a non-negligible computational effort. On the other hand, one could expect smaller differences between the nominal and estimated characteristics than the ones observed in the example studied here, which is a rather extreme and peculiar case.

Yet another possible application of the present method is concerned with the extraction of aerodynamic coefficients from CFD simulations. For example, it would be interesting to try to estimate by this method the three-dimensional correction due to the centrifugal pumping and Coriolis effects (see Lindenburg, 2004). Several works have documented in the literature the direct computation of airfoil polars from the local distribution of pressure and velocity. Unfortunately however, the computation of the effective sectional angle of attack turns out to be a not obvious task (see Shen et al., 2009), so that the estimation procedure proposed in this work could provide for an interesting alternative.

Acknowledgments

Wind tunnel test data was obtained with the help of Dr. Filippo Campagnolo, whose collaboration is here gratefully acknowledged. The aeroelastic wind turbine model was developed with the financial support of Vestas Wind Systems A/S.

References

Abbott, I.H., von Doenhoff, A.E., 1959. Theory of Wing Sections, Including a Summary of Airfoil Data. Dover Publication, Inc., Mineola, NY, USA.

Althaus, D., 1988. ProfilPolaren für den Modellflug. Necktar-Verlag, Vs-Villingen. (in German).

Bahaj, A.S., Molland, A.F., Chaplin, J.R., Batten, W.M.J., 2007. Power and thrust measurements of marine current turbines under various hydrodynamic flow conditions in a cavitation tunnel and a towing tank. Renew. Energy 32 (3), 407–426.

Bak, C., Fuglsang, P., Sørensen, N.N., Madsen, H.A., Shen, W.Z., Sørensen, J.N., 1999. Airfoil Characteristic for Wind Turbines. Technical Report Risø-R-1065(EN), Risø National Laboratory, Roskilde, Denmark.

Bauchau, O.A., Bottasso, C.L., Nikishkov, Y.G., 2001. Modeling rotorcraft dynamics with finite element multibody procedures. Math. Comput. Modell. 33 (10–11), 1113–1137.

Bottasso, C.L., Cacciola, S., Croce, A., 2013a. Estimation of blade structural properties from experimental data. Wind Energy 16 (4), 501–518.
Bottasso, C.L., Campagnolo, F., Petrović, V., 2013b. Wind tunnel testing of scaled wind turbine models: beyond aerodynamics. Renew. Energy, under review.
Bottasso, C.L., Croce, A., 2006–2013. `Cp-Lambda`: User's Manual. Dipartimento di Scienze e Tecnologie Aerospaziali, Politecnico di Milano, Milano, Italy.
Churchfield, M.J., Lee, S., Moriarty, P.J., Martinez, L.A., Leonardi, S., Vijayakumar, G., Brasseur, J.G., 2012. A large eddy simulation of wind-plant aerodynamics. In: Proceedings of 50th AIAA Aerospace Sciences Meeting, Nashville, TN, USA.
Churchfield, M.J., Lee, S., 2012. NWTC design codes (SOWFA). ⟨http://wind.nrel.gov/designcodes/simulators/SOWFA/⟩. Accessed 14 March 2012.
Cramér, H., 1946. Mathematical Methods of Statistics. Princeton University Press, Princeton, NJ, USA.
Drela, M., Giles, M.B., 1987. Viscous-inviscid analysis of transonic and low Reynolds number airfoils. AIAA J. 25 (10), 1347–1355.
Fleming, P., Lee, S., Churchfield, M., Scholbrock, A., Michalakes, J., Johnson, K., Moriarty, P., Gebraad, P., van Wingerden, J., 2013. The SOWFA super-controller: a high-fidelity tool for evaluating wind plant control approaches. In: EWEA 2013 Annual Event, Vienna, Austria.
Gill, P.E., Murray, W., Wright, M.H., 1981. Practical Optimization. Academic Press, London.
Golub, G.H., van Loan, C.F., 1996. Matrix Computations. Johns Hopkins University Press, Baltimore, MD, USA.
Hansen, M.O.L., 2008. Aerodynamics of Wind Turbines. Earthscan, London, UK.
Jategaonkar, R.V., 2006. Flight Vehicle System Identification: A Time Domain Methodology. AIAA Education Series. Reston, VA, USA.
Khalil, W., Dombre, E., 2002. Modeling, Identification and Control of Robots. Hermes Pelton Science, London, UK.
Klein, V., Morelli, E.A., 2006. Aircraft System Identification, Theory and Practice. AIAA Education Series. Reston, VA, USA.
Lancaster, P., Tismenetsky, M., 1985. The Theory of Matrices: With Applications, second ed. Academic Press, Orlando, FL, USA.
Lindenburg, E., 2004. Modeling of rotational augmentation based on engineering consideration and measurements. In: Proceedings of the European Wind Energy Conference & Exhibition (EWEC), London, GB, 22–25 November.
Ljung, L., 1999. System Identification: Theory for the User. Prentice Hall, Englewood Cliffs, NJ, USA.
Olesen, N.A., 2009. Personal communication. Vestas Wind Systems A/S, Aarhus, Denmark.
Peters, D.A., 2009. How dynamic inflow survives in the competitive world of rotorcraft aerodynamics. J. Am. Helicopter Soc. 53 (1), 1–15.
Schepers, J.G., 2012. Engineering Models in Wind Energy Aerodynamics: Development, Implementation and Analysis using Dedicated Aerodynamic Measurements (Ph.D. thesis). Delft University of Technology.
Schito, P., 2011. Large Eddy Simulation of Wind Turbines: Interaction with Turbulent Flow (Ph.D. thesis). Politecnico di Milano.
Shen, W.Z., Hansen, M.O.L., Sørensen, J.N., 2009. Determination of the angle of attack on rotor blades. Wind Energy 12 (1), 91–98.
Sheu, S.Y., Walker, M.W., 1991. Identifying the independent inertial parameter space of robot manipulators. Int. J. Robot. Res. 10 (6), 668–680.
Shome, S.S., Beale, D.G., Wang, D., 1998. A general method for estimating dynamic parameters of spatial mechanism. Nonlinear Dyn. 16 (4), 349–368.
Waiboer, R., 2007. Dynamic Modelling, Identification and Simulation of Industrial Robots — for Off-Line Programming of Robotised Laser Welding (Ph.D. thesis). Netherlands Institute for Metals Research.
Wu, Y.T., Porté-Agel, F., 2011. Large-eddy simulation of wind-turbine wakes: evaluation of turbine parametrisations. Bound. Layer Meteorol. 138 (3), 345–366.